Nano Energy 26 (2016) 313–323

Contents lists available at ScienceDirect

Nano Energy

journal homepage: www.elsevier.com/locate/nanoen

Engineering sulfur vacancies and impurities in $NiCo_2S_4$ nanostructures toward optimal supercapacitive performance

Fei Lu [a], Min Zhou [a,b,*], Wanrong Li [a], Qunhong Weng [b], Cuiling Li [b], Yanming Xue [b], Xiangfen Jiang [b], Xianghua Zeng [a,**], Yoshio Bando [b], Dmitri Golberg [b,**]

[a] College of Physical Science and Technology, and Institute of Optoelectronic Technology, Yangzhou University, Yangzhou 225002, China
[b] World Premier International Center for Materials Nanoarchitectonics (WPI-MANA), National Institute for Materials Science (NIMS), Namiki 1-1, Tsukuba 305-0044, Japan

ARTICLE INFO

Article history:
Received 2 April 2016
Received in revised form
18 May 2016
Accepted 26 May 2016
Available online 27 May 2016

Keywords:
Pseudocapacitor
Transition metal sulfide
Sulfur vacancy
Controlled sulfurization
Solid-state supercapacitor

ABSTRACT

High efficiency supercapacitors require the electrode materials which integrate high specific capacitance, favorable rate capability and long-term cyclic stability. These features are often associated with vacancies and impurities in the electrodes. Understanding the mechanism behind the related process provides a deep insight into improved supercapacitive performance. Here we present the synthesis of spinel structured nickel cobalt sulfide ($NiCo_2S_4$) nanomaterials with tunable sulfur vacancy concentrations and impurities by controlling the sulfurization process. The effects of these defects on the nanomaterial supercapacitive properties were then clearly identified. Interestingly, on one hand, the sulfur vacancies were found to increase the specific capacitance by improving electrical conductivity, while, on the other hand, they hindered the rate capability and cyclic stability due to the increased crystal structure disordering. An optimal supercapacitive performance was achieved, namely, high specific capacitance, favorable rate capability and long-term cyclic stability were documented for both three-electrode system and solid-state asymmetric supercapacitor device. These results have significant implications for the design and optimization of pseudocapacitive properties of transition metal compounds.

1. Introduction

Electrochemical supercapacitors are attractive candidates for the next-generation energy storage devices because of their high power density during a discharging process [1–6]. Pseudocapacitors, in which energy is stored through reversible Faradaic reactions on the electrode materials, possess larger specific capacitance than electrical double-layer capacitors [7–9]. However, the poor charge transfer ability in pseudocapacitive materials, such as transition metal oxides and hydroxides, prevents these systems from applications that require high rate charging and discharging [10,11].

Shortening the charge transfer distance and improving the intrinsic conductivity of electrode materials are two strategies commonly employed to facilitate the charge transfer in pseudocapacitors [12]. The former refers to, for example, in-situ growth of pseudocapacitive materials onto conductive substrates, such as graphene, carbon fibers and nickel foam [11,13–15]. Despite remarkable improvements which have been evidenced with respect to those hybrid electrodes, the promotion of intrinsic conductivity of pseudocapacitive materials is still a challenge. Recently, defect engineering on transition metal oxides has been reported as an effective route to improve their intrinsic conductivity. For instance, Lu and co-workers found that oxygen-deficient α-Fe_2O_3 nanorods had shown an enhanced electrochemical performance compared to that of pristine α-Fe_2O_3, which was due to the increased donor density and number of active sites resulted from the oxygen vacancies [16]. Another example was demonstrated by Li and co-workers, who obtained an improved supercapacitive performance from $NiCo_2O_4$ hollow spheres combining large surface area and high conductivity. A hydrogenation process was employed to increase oxygen vacancies in the electrode material, and therefore to lower the internal resistance as well as the Warburg impedance [12]. Other reports suggested that the introduction of defects, nevertheless, is usually associated with the crystalline structure disordering, which is adverse to the rate capability and cyclic performance [17,18]. In this regard, a synthetic assessment on the defect-related pseudocapacitive performance, including specific capacitance, rate capability and cyclic stability, is desired and of prime significance.

* Corresponding author at: College of Physical Science and Technology, and Institute of Optoelectronic Technology, Yangzhou University, Yangzhou 225002, China.
** Corresponding authors.
E-mail addresses: minzhou@yzu.edu.cn (M. Zhou), xhzeng@yzu.edu.cn (X. Zeng), GOLBERG.Dmitri@nims.go.jp (D. Golberg).

http://dx.doi.org/10.1016/j.nanoen.2016.05.042
2211-2855/

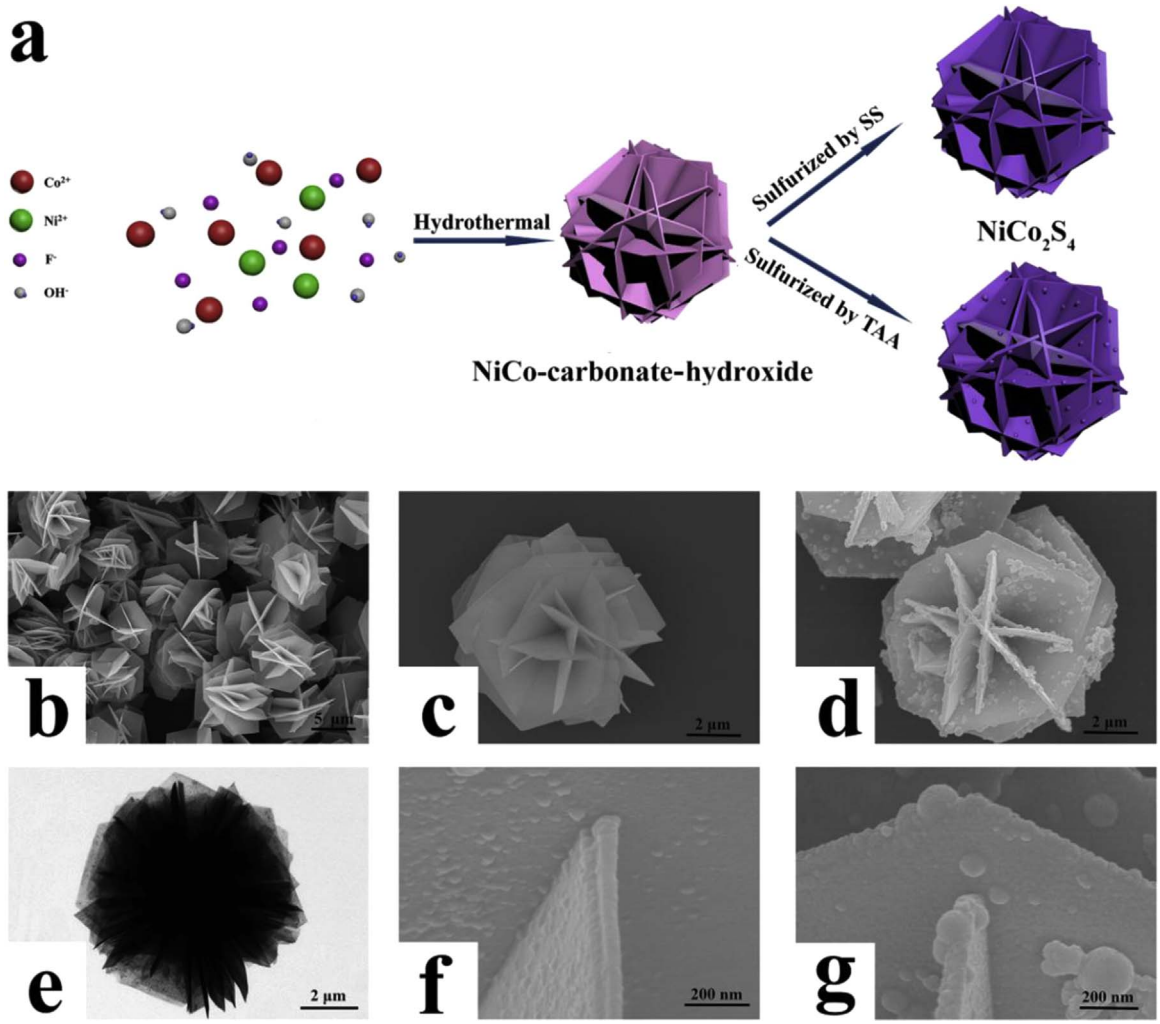

Fig. 1. (a) Schematic illustration of the formation process of $NiCo_2S_4$ nanostructure assembled as nanoflakes, (b) SEM and (e) TEM images of NiCo-precursors, SEM images with varied magnification of (c, f) SS-6 and (d, g) TAA-6 samples.

Mixed valence transition metal oxides and sulfides have been extensively studied as electrode materials in supercapacitors [19]. Specifically, spinel structured nickel-cobalt sulfide ($NiCo_2S_4$) displayed a distinguished electrochemical performance because of its intriguing features of multiple Faradaic reactions and, more importantly, superior conductivity compared with other pseudocapacitive materials [4,8,20–23]. Recent reports have revealed that oxygen vacancies in spinel structured $NiCo_2O_4$ are critical for electrochemical processes in it [12,24]. Considering the similar crystalline structure between $NiCo_2S_4$ and $NiCo_2O_4$ phases [25], it is reasonable to anticipate that sulfur vacancies in nickel cobalt sulfides could play the key roles in tuning their pseudocapacitive properties, which up to now have not been properly considered. Furthermore, various synthetic methods employed in the synthesis of $NiCo_2S_4$ led to the crystallization difference, e.g. defects and impurities [22,25]. Due to the lack of consistency among the various experimental results, the optimal synthetic conditions for nickel cobalt sulfides fabrication towards superior supercapacitive performance have not been identified yet.

In this study, we present the controlled sulfurization of three dimensional (3D) $NiCo_2S_4$ nanostructures, in which the sulfur vacancy concentration and impurities were engineered by varying the sulfur source and sulfurization duration. The effects of sulfur vacancy concentration and impurities on the material supercapacitive performance were clearly identified. Interestingly, we found that the sulfur vacancies improved the specific capacitance of the electrode, yet decreased the rate capability as well as cyclic stability at the same time. The resulted supercapacitive performance was tuned based on the competitive mechanisms of charge transfer ability and disordering of the crystal structure. An optimal supercapacitive performance integrating high specific capacitance, favorable rate capability and long-term cyclic stability was finally realized. This research not only uncovers the optimal sulfurization conditions for the spinel nickel cobalt sulfides, but also shows effective routes to tune the supercapacitive performance, such as specific capacitance, rate capability and cyclic stability of the electrode.

2. Experimental section

2.1. Synthesis of 3D-structured NiCo-carbonate-hydroxide

All chemicals were of analytical grade and were used without further purification. In a typical synthesis of a NiCo-carbonate-hydroxide precursor, 2 mmol $Co(NO_3)_2$, 1 mmol $Ni(NO_3)_2$, 15 mmol urea and 6 mmol NH_4F were dissolved into 35 ml distilled water to form a transparent pink solution. This aqueous solution was then transferred into a 46 ml Teflon-lined stainless steel autoclave and kept at 100 °C for 3.5 h. After cooling to room temperature naturally, the purple precipitate was separated under centrifugation in distilled water and ethanol several times, and vacuum dried at 80 °C for 6 h.

2.2. *Synthesis of 3D-structured $NiCo_2S_4$*

The as-synthesized NiCo-precursor was then sulfurized by thioacetamide (TAA) or sodium sulfide (SS) over various times. In a typical synthesis of $NiCo_2S_4$ treated by TAA, 30 mg of the NiCo-precursor was re-dispersed in 20 ml ethanol, followed by dissolution of 50 mg TAA as a sulfur source. Then the suspension was transferred into a 46 ml Teflon-lined stainless steel autoclave and kept at 180 °C for 6 h or 12 h. After centrifugation with ethanol for several times and vacuum drying at 60 °C overnight, the 3D-structured $NiCo_2S_4$ was obtained. These samples were abbreviated as TAA-6 and TAA-12. In the case of samples sulfurized by Na_2S, TAA and ethanol were replaced by identical amount of Na_2S and distilled water, respectively. The sulfurization was conducted for 6, 12 and 24 h, and the resulted samples were named as SS-6, SS-12, SS-24, respectively.

2.3. *Structural characterization*

The as-prepared nickel cobalt sulfides were characterized using a Hitachi S4800 field-emission scanning electron microscope (SEM) with a Thermo Noran energy-dispersive X-ray spectrometer (EDS), and Shimadzu XRD-7000 powder X-ray Diffractometer (XRD) with monochromatized Cu Ka irradiation. Raman spectra were measured with a Renishaw inVia Raman spectrometer having an excitation wavelength of 532 nm. The high-resolution transmission electron microscopy (HRTEM) and selected area electron diffraction (SAED) were carried out on a Tecnai G2 F30 S-TWIN instrument at the accelerating voltage of 300 kV, accompanied with EDXA energy-dispersive X-ray mapping (EDS mapping) for element distribution analysis. High-resolution XPS measurements for evaluation of elemental species and their chemical states were carried out on a Thermo ESCALAB250Xi with a resolution of 0.43 eV.

2.4. *Electrochemical measurements*

The electrochemical measurements were conducted in a three-electrode electrochemical cell with Pt foil as a counter electrode and saturated calomel electrode as a reference electrode in 6 M KOH aqueous solution. The working electrode was prepared by mixing the as-prepared samples, conductive graphite and PTFE at a mass ratio of 85:10:5. The slurry was coated onto cleansed nickel foam and vacuum dried overnight. The supercapacitive performance was estimated on a CHI 660E (Chenhua, Shanghai) electrochemical workstation by using cyclic voltammetry, galvanostatic charge-discharge and AC impedance techniques. The mass loadings of the as-prepared samples in the electrodes were 1.97, 1.83, 1.95, 1.86 and 2.00 mg/cm^2 for SS-6, SS-12, SS-24, TAA-6 and TAA-12, respectively. The calculation method of the specific capacitance is presented in the Supplementary material.

The relative electrochemical active surface areas (REASA) were estimated by probing the electrochemical-double-layer specific capacitances of the electrodes. The electrochemical-double-layer specific capacitances were extracted from cyclic voltammetry curves at non-Faradaic potentials region (-0.4 to -0.2 V vs SCE in this study) according to Eq. S1 in the Calculation method in the Supplementary material.

2.5. *I-V measurements*

The electrodes were prepared by pressing the as-synthesized samples (20 mg) into a disk (d=0.6 cm) at a pressure of 5 MPa. Then, the samples were sandwiched and firmly pressed with two copper discs (d=0.4 cm) using an insulating clip. The current-voltage (I-V) curves were recorded by a linear sweep voltammetry using CHI 660E electrochemical workstation.

2.6. *Fabrication of all-solid-state asymmetric supercapacitor*

The all-solid-state asymmetric supercapacitor was assembled by separating the $NiCo_2S_4$ (TAA-6 as cathode) and reduced graphene oxide (rGO) hydrogel (anode) by a piece of cellulose paper. Solid-state PVA/KOH gel was employed as electrolyte, which was prepared by dissolving 2.24 g KOH and 4 g PVA in 40 ml H_2O. The masses of cathode and anode materials were 1.78 mg and 8.19 mg, respectively. This proportion was fixed based on the charge balance theory (Eq. S5 in the Supplementary material) and the difference in specific capacitance between TAA-6 and rGO hydrogel (Fig. S11). Before assembling, each electrode was coated with a PVA/KOH gel. The asymmetric device was fabricated by sandwiching the separator between the cathode and anode. After drying, the assembled device was finally encapsulated into lithium ion battery housing. Electrochemical measurements including cyclic voltammetry, galvanostatic charge-discharge cycles, AC

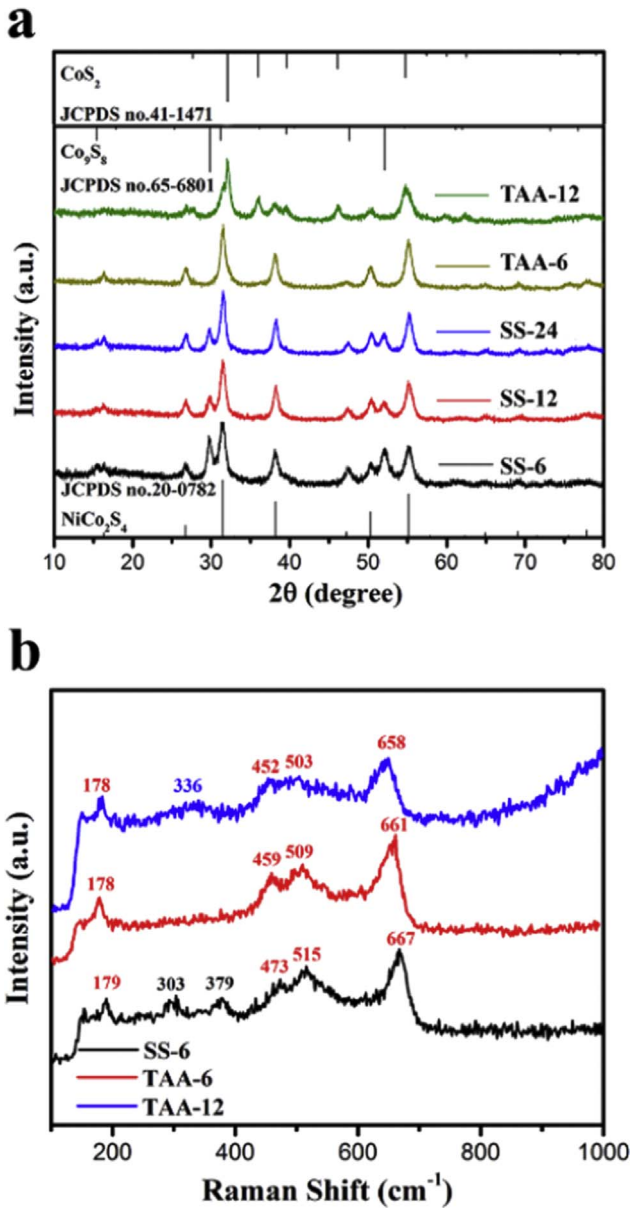

Fig. 2. (a) XRD patterns of as-prepared samples, and (b) Raman spectra of SS-6, TAA-6 and TAA-12 samples.

impedance and self-discharge measurements were conducted to estimate the performance of the asymmetric supercapacitor.

3. Results and discussion

3.1. Preparation and characterization

The 3D $NiCo_2S_4$ structures were synthesized via a two-step process, as illustrated in Fig. 1a. In the first step, a uniform 3D structured NiCo-carbonate-hydroxide was obtained via a simple hydrothermal method. SEM and TEM images (Fig. 1b and e) show that the precursors are 4–5 μm in diameter and are assembled as nanoflakes with a thickness of about 30 nm. Secondly, the $NiCo_2S_4$ structures were sulfurized by varying the sulfur sources (TAA or SS) and the sulfurization durations (6 h, 12 h or 24 h). The hierarchical morphology of 3D $NiCo_2S_4$ nanostructure was well inherited from the precursor by using either TAA or SS as a sulfide source (Fig. 1c and d). Nevertheless, thicker flakes were observed in the $NiCo_2S_4$ samples compared with those in the precursor, especially for the samples sulfurized by TAA (Fig. 1f and g), indicating a volume expansion process during the sulfurization.

The XRD pattern of sample TAA-6 in Fig. 2a was indexed to the spinel phase of $NiCo_2S_4$ (JCPDS card no. 43-1477) without any residues and contaminants, indicating that the NiCo-carbonate-hydroxide precursor was totally converted into $NiCo_2S_4$. Some additional peaks indexed to cubic Co_9S_8 phase (JCPDS card no. 65-6801) were observed from sample SS-6 besides the primary diffraction peaks of $NiCo_2S_4$ spinel. The existence of Co_9S_8 phase suggests the incomplete sulfurization of the samples using Na_2S as a sulfur source, which was also verified by previous reports [23,26]. Notably, extending the sulfurization time to 24 h leads to increased crystallinity as well as volume expansion of the nanoflakes (Fig. 2a and Fig. S1), but does not eliminate the Co_9S_8 phase impurity from the samples. On the other hand, prolonging the sulfurization duration in the TAA system results in another CoS_2 impurity (JCPDS card no. 41-1471), as shown in the XRD pattern of TAA-12, which is ascribed to over-sulfurization of the sample. Moreover, the sulfur content in the samples varies, while the proportion of nickel and cobalt keeps constant at 0.5 (EDS in Fig. S2), implying the difference in sulfurization state among the samples.

The structure features were also detected by Raman spectra (Fig. 2b), in which the peaks centered at 178, 459, 509, and 661 cm^{-1} are ascribed to F_{2g}, E_{2g}, F_{2g}, and A_{1g} modes of $NiCo_2S_4$, respectively. Compared with the typical stretching vibration from TAA-6, a blue shift of the peak location is observed from SS-6, while it is red shifted in the case of TAA-12. These peak shifts may be interpreted by the variation of the dimensional scale since there is difference in volume expansion among different samples [27]. Furthermore, the introduced impurities in SS-6 and TAA-12 were also confirmed by Raman spectra. The prominent peaks located at 303 and 379 cm^{-1} from SS-6 are related to the stretching vibration of Co_9S_8, and the pronounced band centered at 336 cm^{-1} is assigned to the characteristic stretching vibration of CoS_2 phase [28–30].

Fig. 3a shows the HRTEM image of a $NiCo_2S_4$ nanoflake from sample TAA-6. The measured interplanar d-spacings of 0.16, 0.28, 0.33 and 0.53 nm can be readily indexed to (531), (311), (220) and (111) crystal planes of $NiCo_2S_4$. The interlaced crystalline directions suggest the polycrystalline nature of the sample, which is also confirmed by the annular patterns in the SAED image (Fig. 3b). A EDX mapping displayed in Fig. 3c reveals a homogeneous distribution of Ni, Co and S in TAA-6. Additionally, we detected the Co_9S_8 phase in SS-6 and CoS_2 phase in TAA-12 (Fig. S3). These are consistent with the results obtained from XRD and Raman spectra. It is noted that Ni and Co are distributed uniformly even in SS-6 and TAA-12, in spite of the impurities introduced (Fig. S4). Therefore, the Co_9S_8 phase and CoS_2 phase impurities are considered to actually be $(Ni/Co)_9S_8$ and $(Ni/Co)S_2$, respectively, in which the cationic positions in the crystal cell are randomly occupied by Ni and Co.

The variation of sulfurization conditions not only introduces impurities, but also leads to difference in sulfur vacancy concentrations in the samples. In the XPS spectra of S 2p for each sample (Fig. 4a), the peak at the lower binding energy corresponds to S $2p_{3/2}$ core level, this is attributed to typical metal-sulfur bonds [8,23], while the peak of S $2p_{1/2}$ at the higher energy is assigned to sulfur with low coordination, which is generally related to sulfur vacancies [31]. The relative intensity of $2p_{1/2}$ in S 2p spectrum is 48.2% for TAA-6. This proportion increases to 57.8% for SS-6, indicating a higher sulfur vacancy concentration in SS-6,

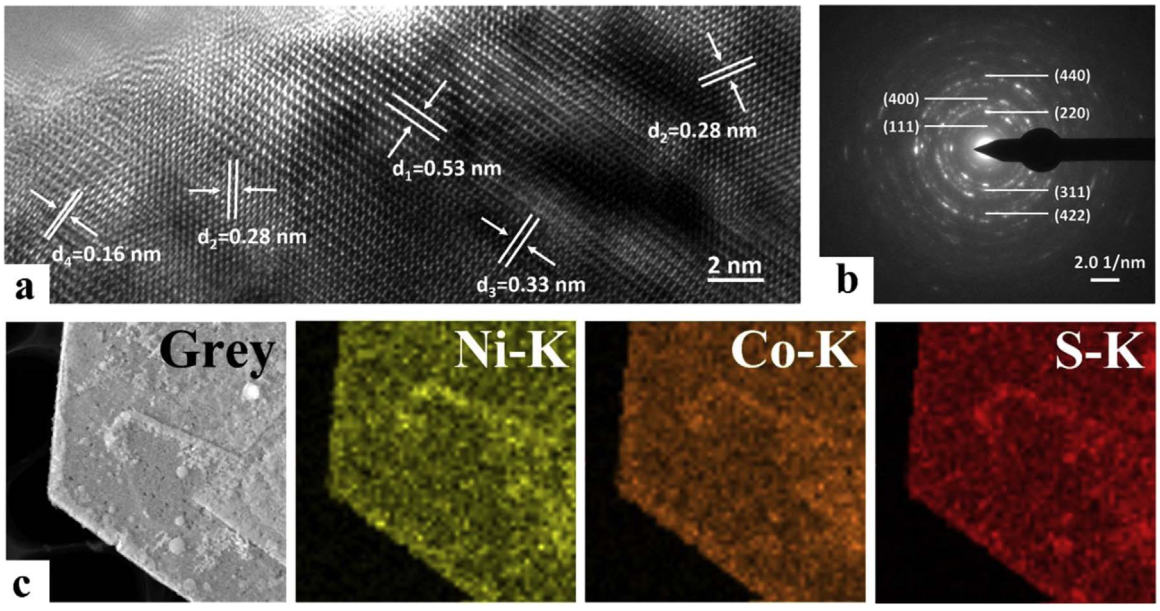

Fig. 3. (a) HRTEM images, (b) SAED pattern and (c) elemental mapping of a TAA-6 sample.

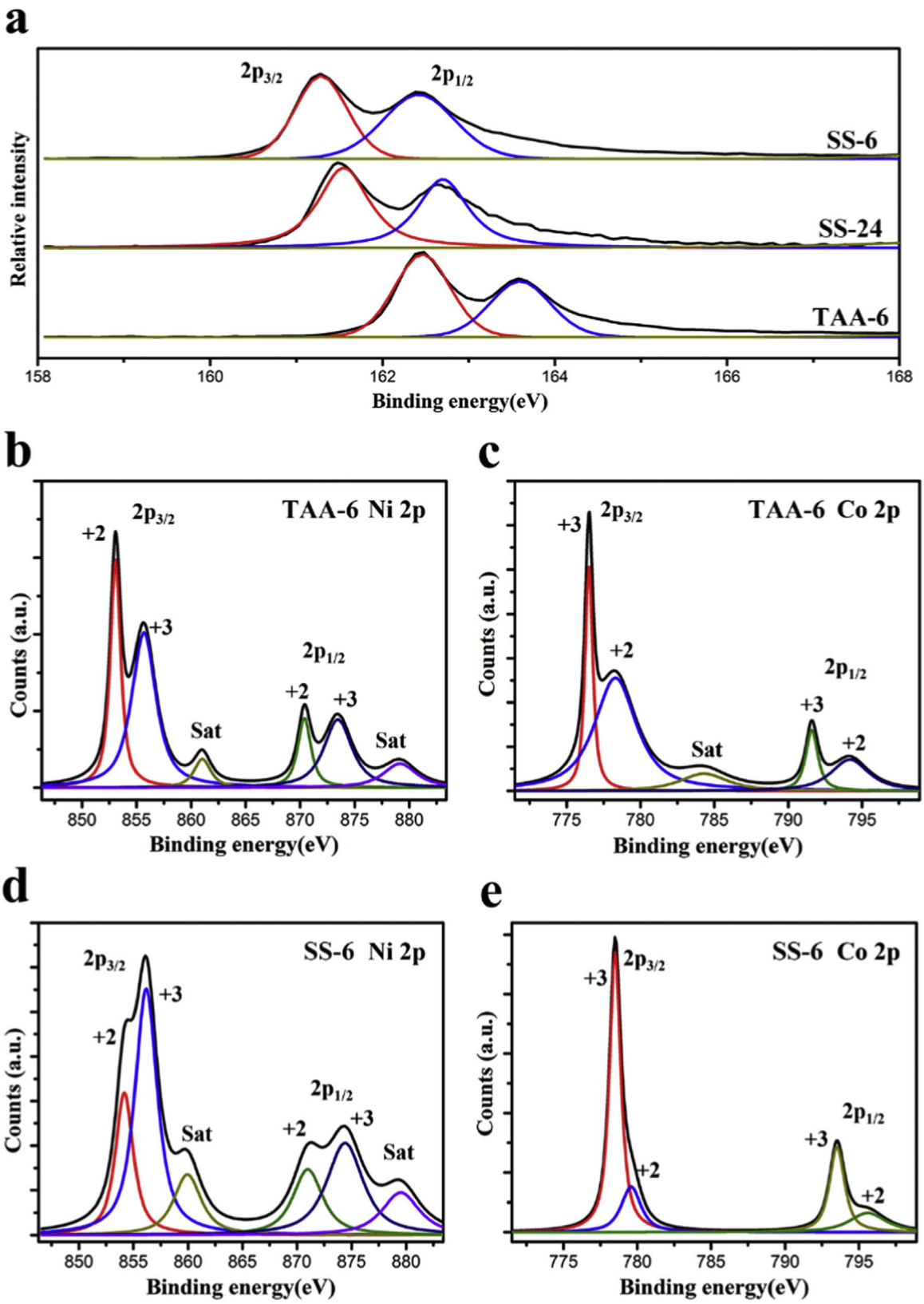

Fig. 4. Binding energy of the nickel cobalt sulfide. (a) Normalized S 2p core level XPS spectra of SS-6, SS-24 and TAA-6 samples, (b, c) high resolution XPS spectra of Ni 2p and Co 2p of SS-6, and (d, e) high resolution XPS spectra of Ni 2p and Co 2p of TAA-6 sample.

which is caused by the insufficient sulfurization of the samples treated by Na_2S. Moreover, the relative intensity of $2p_{1/2}$ declines gradually from SS-6 to SS-24, implying that the amount of sulfur vacancies can also be controlled by the sulfurization time. The variation of sulfur vacancy concentration was also verified by the changes of cationic valence. Compared to the pristine sample TAA-6, the sample SS-6 exhibits the higher relative intensities of Ni^{2+} and Co^{2+}, while the lower intensities of Ni^{3+} and

Co^{3+}. This indicates a higher sulfur vacancy concentration in SS-6 (Fig. 4b–e).

3.2. Electrochemical performance in three-electrode system

The electrochemical performances of the as-synthesized samples were tested for working electrodes in supercapacitors within a three-electrode system. Cyclic voltammetric (CV) curve of each sample displays typical redox peaks (Fig. 5a), which are obviously distinct from electrical double-layer capacitance characterized as rectangular curves. The pseudocapacitive features of $NiCo_2S_4$ come from the Faradaic redox reactions, as illustrated by the following equations: [32].

$$NiCo_2S_4 + OH^- + H_2O \leftrightarrow NiS_{4-4x}OH + 2CoS_{2x}OH + e^- \quad (1)$$

$$CoS_{2x}OH + OH^- \leftrightarrow CoS_{2x}O + H_2O + e^- \quad (2)$$

$$CoS_{2x} + OH^- \leftrightarrow CoS_{2x}OH + e^- \quad (3)$$

$$NiS_{4-4x} + OH^- \leftrightarrow NiS_{4-4x}OH + e^- \quad (4)$$

The shape of CV curves is ideally retained after the scan rate increased to 100 mV/s (Fig. 5b and Fig. S6), indicating ideal rate capabilities of the samples. Furthermore, with the scan rate varying from 10 to 100 mV/s, the anodic peaks shift to a higher potential while the cathodic peaks move to a lower potential. This is due to the insufficient intercalation of ions from electrolyte into the dense center of $NiCo_2S_4$ [33]. For a qualitative comparison, the relationship between scan rate and current density of each sample was plotted, as shown in Fig. 5(c). Generally, the peak current (I) in the CV curves follows a power-law with changing of scan rate (v), as described by the equation: [34].

$$I = av^b \quad (5)$$

where the coefficient 'a' and exponent 'b' are adjustable. In the case of b=0. 5, the electrochemical process is considered to be diffusion-controlled, while b=1 indicates a surface-controlled process. As described in Fig. 5c, the anodic peak current for each sample increases ideally linearly with increasing the scan rate, implying that the electrochemical process in the electrodes is surface-controlled.

Galvanostatic charge-discharge (GCD) measurements were carried out at various current densities to extract specific capacitances for all samples (Fig. 6a and Fig. S7). The calculated specific capacitances of SS-6, SS-12, SS-24, TAA-6, and TAA-12 are 2363.1, 2092.5, 1625.6, 2141.9, and 1236.9 F/g at the current density of 2.5 A/g, respectively. The sample SS-6 displays the highest capacitance among all samples, followed by TAA-6. However, this trend is changed at the higher current densities, e.g. 40 A/g (Fig. 6b). 82.2% of the initial specific capacitance is retained for TAA-6 (1760.0 F/g at 40 A/g), which is higher than 68.1% for SS-6 (1610.0 F/g at 40 A/g), indicating a superior rate capability of TAA-6. The specific capacitance of each sample was also calculated based on the CV curves, which suggest similar trends both on the initial capacitance and rate capability (Fig. S8). In addition to favorable rate capability, the pristine $NiCo_2S_4$ (TAA-6) also showed a distinguished cyclic stability at a high current density of 62.5 A/g (Fig. 6c). A negligible loss in capacitance was observed from TAA-6 after 5000 cycles (99.3% capacitance retained), in contrast to 75.1% capacitance retained for SS-6. It is worth noting that the supercapacitive performance of TAA-6 is among the best of the reported

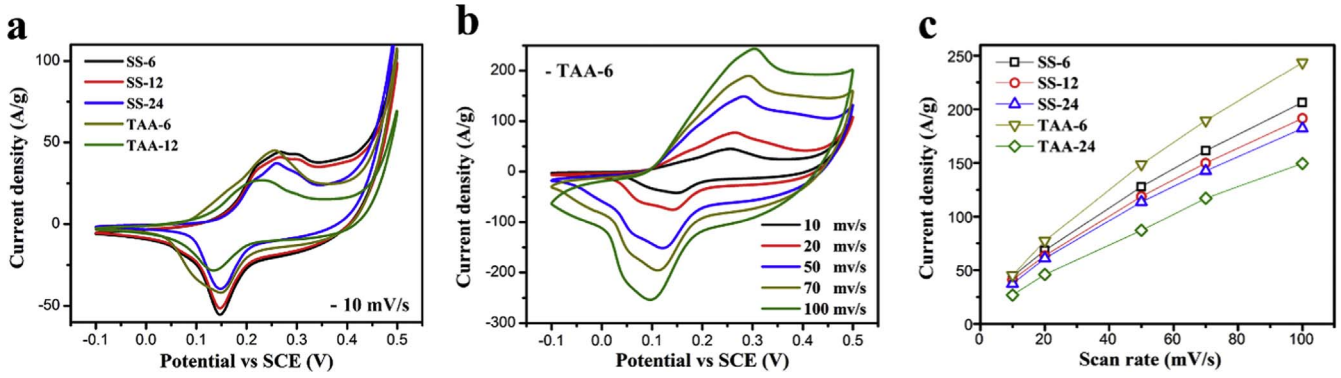

Fig. 5. CV performance of the samples. (a) CV curves of all samples at a scan rate of 10 mv/s, (b) CV curves of TAA-6 sample at varied scan rates, and (c) the anodic peak current density of all samples as a function of scan rate.

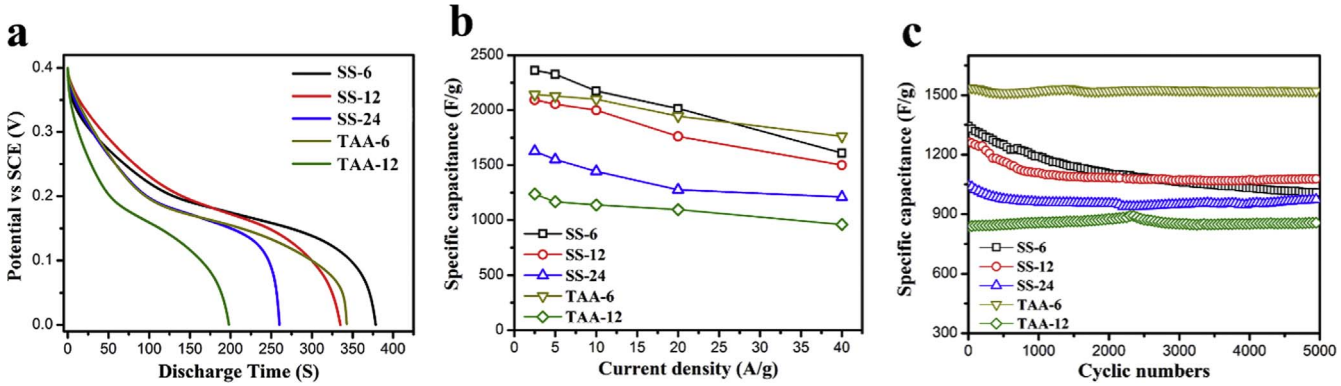

Fig. 6. (a) GCD curves of all samples at a current density of 2.5 A/g, (b) calculated specific capacitance of all samples as a function of current density, and (c) cyclic stability of all samples at a current density of 62.5 A/g.

results from nickel cobalt sulfides, and even comparable to that of samples in-situ grown on conductive substrates (Table S1) [21,23,35–42].

3.3. Discussion

The outstanding supercapacitive properties of TAA-6 are benefited from the rational optimization of $NiCo_2S_4$ nanomaterials. However, the origin of difference in electrochemical properties among various samples is still unrevealed. The performance of the electrode materials in a supercapacitor is generally limited by the density and reactivity of active sites and their charge transfer abilities. Therefore, impurities, surface area and electrical conductivity are considered to be crucial factors related to their supercapacitive properties. The impurities, as $(Ni/Co)_9S_8$ and $(Ni/Co)S_2$ phases, may cause a decline in the capacitance since the reported capacitances of both are inferior to $NiCo_2S_4$ [23,43–47]. However, the capacitance of SS-6 is larger than that of the pristine sample (TAA-6), and also larger than those of SS-12 and SS-24 samples, which contain $(Ni/Co)_9S_8$ phase as well. This implies that the specific capacitance is controlled by some other factors in addition to the impurities.

The surface area, on the other hand, should be nearly the same among various samples since they were transformed from the same precursor, and have similar morphology, despite slight changes in the thickness of the nanoflakes. This assumption is supported by the measurements of REASA (Fig. 7a). The electrochemical-double-layer specific capacitances were derived from the CV curves at non-Faradaic potentials (Fig. S9), which were used to probe the effective surface areas of each sample during electrochemical process. According to Fig. 7a, there is no obvious distinction for the double-layer capacitance among the samples at different scan rates, indicating that the surface area is not responsible for the supercapacitance variation.

The effect of electrical conductivity on the pseudocapacitive performance was investigated by electrochemical impedance spectroscopy (EIS) measurements (Fig. 8a and b). The Nyquist plots of the samples present semicircles with small diameters in a high frequency range, implying low charge-transfer resistances (R_{ct}) during electrochemical processes [21,22]. The equivalent series resistances (R_{es}), which were derived from the curves intersecting with the real axis, are 0.44, 0.58, 0.63, 0.57 and 0.70 Ω for SS-6, SS-12, SS-24, TAA-6, and TAA-12, respectively. Notably, the conductivity trend is well consistent with the capacitance trend presented above, suggesting a strong correlation between the electrical conductivity and specific capacitance of the samples. Furthermore, the EIS measurements were also performed on SS-6 and TAA-6 before and after the cycles (Fig. 8c and d), since they displayed quite different behaviors in cyclic stability (Fig. 6c). The R_{es} of SS-6 increases from 0.44 to 0.88 Ω, corresponding to the specific capacitance of SS-6 decreasing from 1341.0 to 1009.0 F/g after the cycles. In contrast, a small decrease in conductivity (from 0.58 to 0.60 Ω) is observed in TAA-6, while the specific capacitance remains almost unchanged during the same process. These results revealed that the electrical conductivity is the determining factor in tuning the supercapacitive performance of the samples.

The electrical conductivity data obtained from EIS measurements may be influenced by other factors such as electrolyte, binder, conductive additive and loading mass of the active materials. To get an accurate comparison of the intrinsic electrical conductivity, the I-V curves of the samples were recorded using linear sweep voltammetry (Fig. 7b). The intrinsic electrical conductivity was estimated by means of the I-V curve slopes. Interestingly, the conductivity trend, as derived from I-V curves is SS-6 > TAA-6 > SS-12 > SS-24 > TAA-12, which coincides with the conductivity performance obtained from EIS measurements, and further confirms the crucial effect of electrical conductivity on their supercapacitive performance.

Further study was dedicated to reveal the mechanism behind the varied electrical conductivity among different samples. $NiCo_2S_4$ was

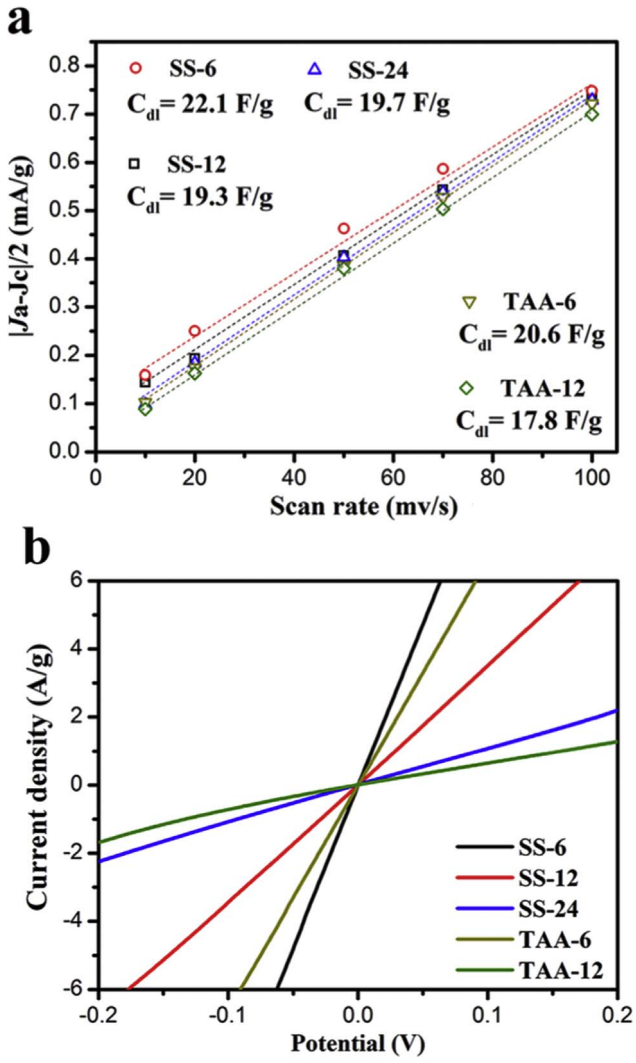

Fig. 7. (a) The extraction of the double-layer capacitance for each sample. (b) The I-V curves of all samples.

reported to be a semiconductor with a band gap of 0.43 eV [48], in which the electrical conductivity is influenced by the amount of charge carriers, and generally associated with defects in a crystal structure. In this study, the conductivity of $NiCo_2S_4$ is considered to be affected by impurities and sulfur vacancies, simultaneously. Firstly, the impurities, either $(Ni/Co)_9S_8$ or $(Ni/Co)S_2$, introduce additional boundaries and interfaces, and hinder the electron transfer in the material. Secondly, the sulfur vacancies provide excess charge carriers as electron donors, thus improving the electrical conductivity in $NiCo_2S_4$. As a result, the resistance of SS-6 is even lower than that of the pristine phase TAA-6, despite the existence of $(Ni/Co)_9S_8$ impurity. Furthermore, the vacancy concentration declines along with the sulfurization time in the Na_2S system, leading to an increase of resistance. The initial specific capacitance therefore depends on the conductivity, and is in the order of SS-6 > TAA-6 > SS-12 > SS-24 > TAA-12.

In addition to the effect on specific capacitance, the sulfur vacancies play another role in regulating the rate capability and cyclic stability of the samples. The vacancy-rich samples, with profound crystal disordering, likely transform into an amorphous phase during the charge-discharge process [12]. This amorphous phase is of a larger resistance compared with that of well-crystalline structures. Therefore, samples that are of high vacancies concentration (SS-6, SS-12 and SS-24) cannot maintain the capacitance at high current density or after long-term cycles due to the increased resistance, as depicted in Fig. 6(b) and (c). Overall, the

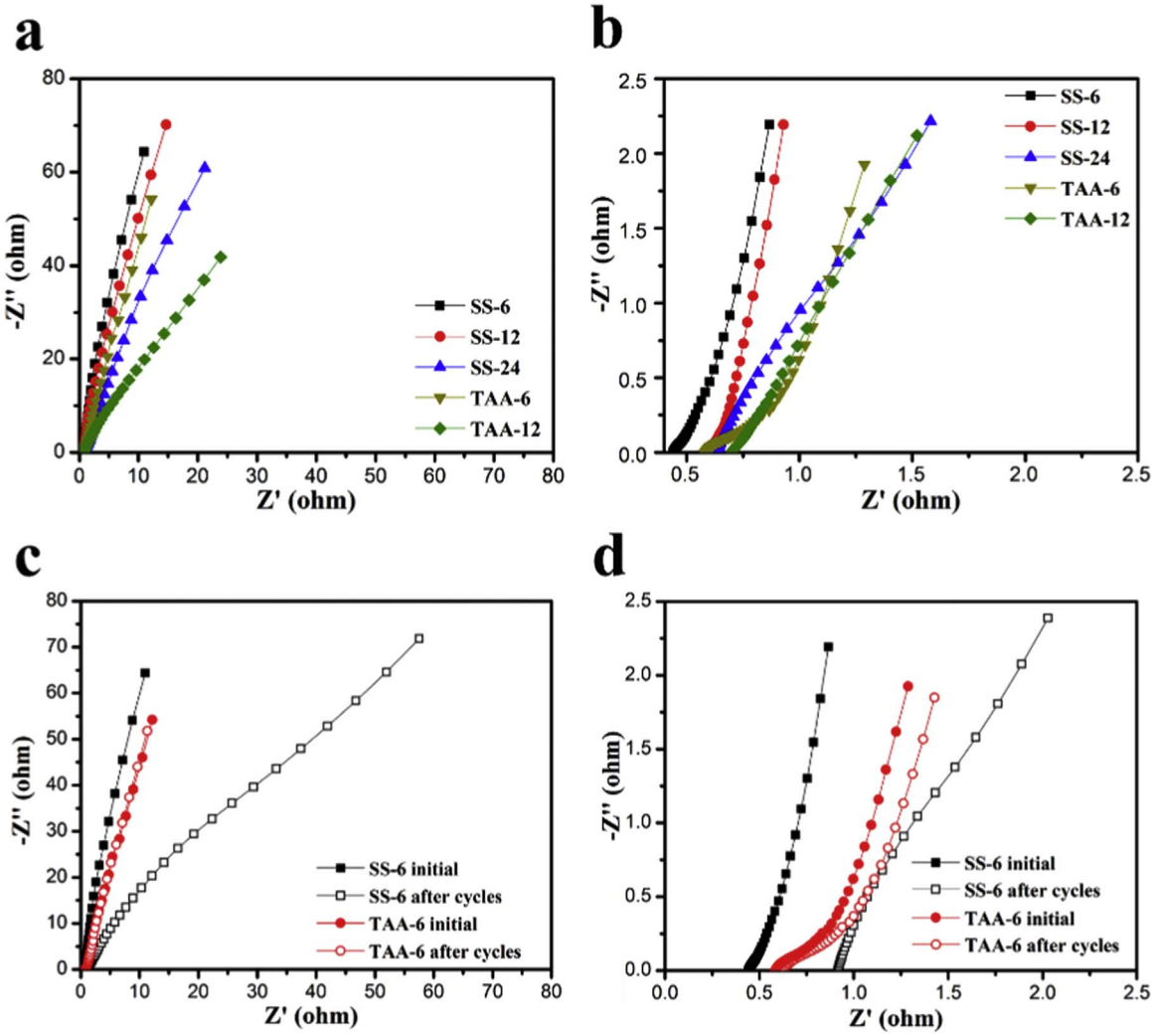

Fig. 8. (a) The EIS curves of all samples, and (c) the EIS spectra of SS-6 and TAA-6 samples after the 1st and 5000th cycles. (b and d), the enlarged EIS spectra of corresponding samples.

pristine phase $NiCo_2S_4$ of TAA-6, integrating low resistance and steady crystal structure, displays the most favorable supercapacitive performance including specific capacitance, rate capability and cyclic stability.

3.4. *Electrochemical performance of all-solid-state asymmetric supercapacitor*

To illustrate the sample practical application potentials, an all-solid-state asymmetric supercapacitor was assembled by using TAA-6 as a cathode and reduced graphene oxide (rGO) hydrogel as an anode. The details of the preparation and characterization of the rGO hydrogel are presented in Fig. S10. The rGO electrode exhibits characteristic electrical double-layer capacitance with a potential window of −1.0 to 0 V, while the working voltage of the cathode varies from −0.1 to 0.5 V (Fig. S11). The working voltage of the assembled asymmetric supercapacitor thus can be extended to 1.5 V. No obvious distortion is observed in the CV curves of the full cell even at a scan rate of 100 mV/s (Fig. 9a), indicating the favorable fast charge-discharge performance of the device. The specific capacitances of the device calculated from the GCD curves (Fig. 9b) are 111.5, 96.9, 87.9, and 81.1 F/g at the current density of 1.6, 3.2, 6.4, and 12.8 A/g, respectively (Fig. 9c). Impressively, 72.7% of the initial specific capacitance was retained after the current density has been increased eightfold, which is consistent with the excellent rate capability of TAA-6 documented for the three-electrode system. Fig. 9d shows the long-term cyclic stability of the asymmetric supercapacitor carried out at the current density of 12.8 A/g. A slight increase of the specific capacitance, at first, is ascribed to the complete activation of the electrode. The specific capacitance still maintains within a stable stage with a small drop after 10,000 cycles, demonstrating the outstanding cyclic stability of the device. The EIS curves measured after the 1st and 10,000th cycles further affirm the superior stability of the device (Fig. S12). More importantly, the Coulombic efficiency of the devices remains of constant value, i.e. 97%, during cycles (Fig. 9d). Besides, the solid-state device exhibits typical self-discharge behavior (Fig. S13). The output voltage of device decreases to 0.66 V after 45,000 s, which is comparable to previous results of solid-state supercapacitors [7,11]. Furthermore, the energy density of 38.64 Wh/kg is obtained at a power density of 1.33 kW/kg. The energy density still remains at 28.48 Wh/kg when the power density increases to 10.79 kW/kg (Fig. 9e). The Ragone plot further demonstrates that the device performance recorded in this work is among the best of the reported results [36–38,49,50]. Dramatically, as many as 36 light-emitting diodes (LED) connected in parallel were lighted at the same time by using three asymmetric supercapacitors connected in series (Fig. 9f), verifying the attractive potential of the present electrode material towards smart practical applications.

4. Conclusions

In summary, 3D $NiCo_2S_4$ structures assembled as nanoflakes were

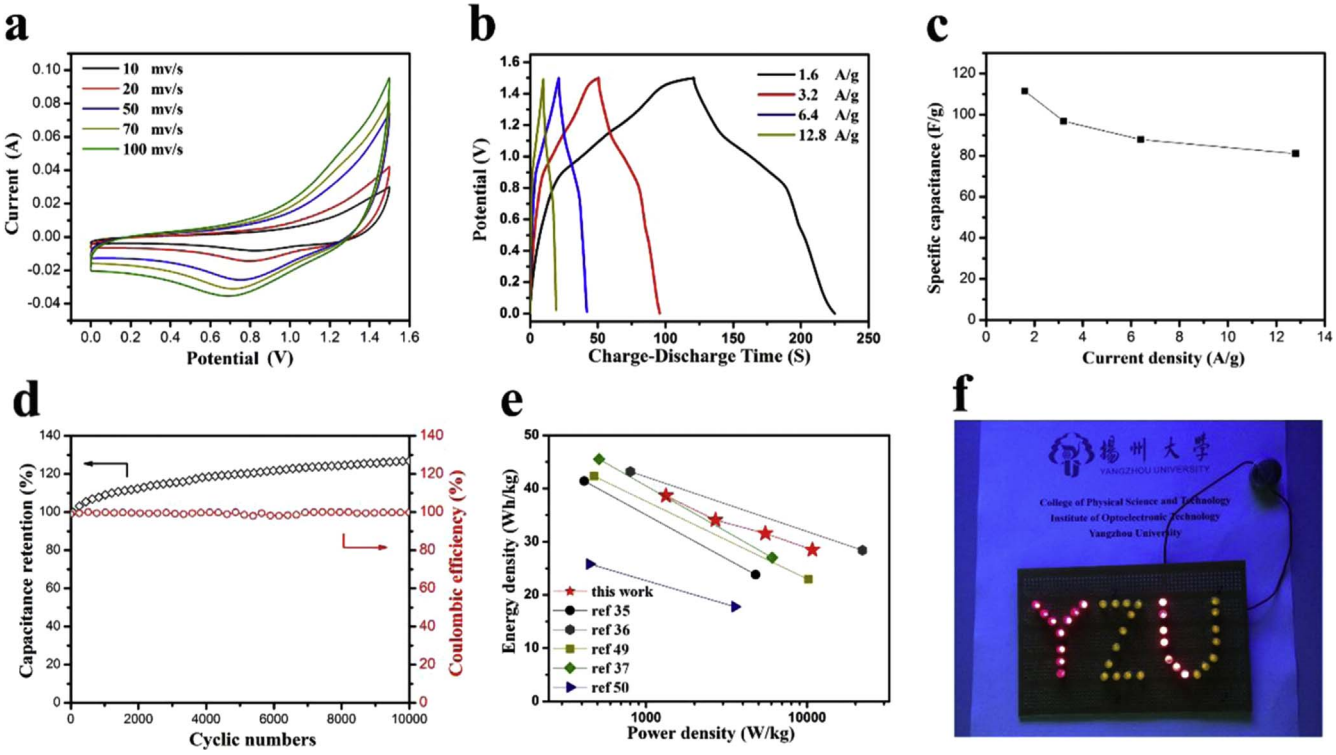

Fig. 9. Electrochemical performance of an all-solid-state asymmetric supercapacitor fabricated by TAA-6 sample and rGO hydrogel as electrodes. (a) CV curves, (b) GCD curves, (c) calculated specific capacitance and (d) cyclic performance and Coulombic efficiency of the asymmetric supercapacitor. The current density is 12.8 A/g in (d). (e) Ragone plot of the solid-state supercapacitors from this work and other related works. (f) A photo of three asymmetric supercapacitors connected in series powering 36 LEDs.

fabricated using a hydrothermal method followed by a sulfurization process. The sulfur vacancies and impurities were controlled by varying the sulfur source and reaction time during the sulfurization process. The roles of sulfur vacancies and impurities in the material supercapacitive properties were clearly identified in terms of specific capacitance, rate capability and cyclic stability. Especially, the specific capacitance benefited from the improved electrical conductivity of the samples, which was caused by introducing sulfur vacancies. These vacancies, however, were found unfavorable for the rate capability and cyclic stability due to the progressed disordering in the crystal structure. A superior supercapacitive performance was documented for the optimized sample sulfurized by TAA for 6 h, the latter integrated a high specific capacitance (2141.9 F/g at the current density of 2.5 A/g), favorable rate capability (82.2% of the capacitance retained at the current density of 40 A/g) and excellent cyclic stability (99.3% of the capacitance retained after 5000 cycles). The outstanding performance was also verified in the all-solid-state asymmetric supercapacitor by using TAA-6 and rGO hydrogel as working electrodes. This work thus proposes a very promising candidate for electrode materials and gives new insights into tuning electrochemical performance of transition metal compound-based supercapacitors.

Acknowledgements

The authors acknowledge the financial support provided by National Natural Science Foundation of China (No. 61301026) and the Research and Innovation Project for College Graduates of Jiangsu Province (KYLX15_1354). We also appreciate the technical support from Testing Center of Yangzhou University. Q.W., C.L., Y.X., X.J., Y.B. and D.G. are grateful to MANA-NIMS for a continuous support.

Appendix A. Supplementary material

Supplementary data associated with this article can be found in the online version at http://dx.doi.org/10.1016/j.nanoen.2016.05.042.

References

[1] M. Dresselhaus, I. Thomas, Nature 414 (2001) 332–337.
[2] G.Z. Chen, Prog. Nat. Sci. 23 (2013) 245–255.
[3] A. Laheäär, P. Przygocki, Q. Abbas, F. Béguin, Electrochem. Commun. 60 (2015) 21–25.
[4] G.Q. Zhang, H.B. Wu, H.E. Hoster, M.B. Chan-Park, X.W.D. Lou, Energy Environ. Sci. 5 (2012) 9453–9456.
[5] X.-F. Jiang, X.-B. Wang, P. Dai, X. Li, Q. Weng, X. Wang, D.-M. Tang, J. Tang, Y. Bando, D. Golberg, Nano Energy 16 (2015) 81–90.
[6] Y. Huang, H. Li, Z. Wang, M. Zhu, Z. Pei, Q. Xue, Y. Huang, C. Zhi, Nano Energy 22 (2016) 422–438.
[7] G. Wang, L. Zhang, J. Zhang, Chem. Soc. Rev. 41 (2012) 797–828.
[8] J. Xiao, L. Wan, S. Yang, F. Xiao, S. Wang, Nano Lett. 14 (2014) 831–838.
[9] Y. Huang, J. Tao, W. Meng, M. Zhu, Y. Huang, Y. Fu, Y. Gao, C. Zhi, Nano Energy 11 (2015) 518–525.
[10] W. Wei, X. Cui, W. Chen, D.G. Ivey, Chem. Soc. Rev. 40 (2011) 1697–1721.
[11] P.J. Hall, M. Mirzaeian, S.I. Fletcher, F.B. Sillars, A.J. Rennie, G.O. Shitta-Bey, G. Wilson, A. Cruden, R. Carter, Energy Environ. Sci. 3 (2010) 1238–1251.
[12] X. Li, L. Jiang, C. Zhou, J. Liu, H. Zeng, NPG Asia Mater. 7 (2015), e165/1–e165/8.
[13] Z. Gao, W. Yang, J. Wang, N. Song, X. Li, Nano Energy 13 (2015) 306–317.
[14] Q. Wang, X. Wang, J. Xu, X. Ouyang, X. Hou, D. Chen, R. Wang, G. Shen, Nano Energy 8 (2014) 44–51.
[15] W. Meng, W. Chen, L. Zhao, Y. Huang, M. Zhu, Y. Huang, Y. Fu, F. Geng, J. Yu, X. Chen, C. Zhi, Nano Energy 8 (2014) 133–140.
[16] X. Lu, Y. Zeng, M. Yu, T. Zhai, C. Liang, S. Xie, M.S. Balogun, Y. Tong, Adv. Mater. 26 (2014) 3148–3155.
[17] R.D.L. Smith, M.S. Prévot, R.D. Fagan, Z. Zhang, P.A. Sedach, M.K.J. Siu, S. Trudel, C.P. Berlinguette, Science 340 (2013) 60–63.
[18] M. Gong, H. Dai, Nano Res. 8 (2015) 23–39.
[19] D.P. Dubal, P. Gomez-Romero, B.R. Sankapal, R. Holze, Nano Energy 11 (2015) 377–399.
[20] X. Yu, B. Lu, Z. Xu, Adv. Mater. 26 (2014) 1044–1051.
[21] W. Chen, C. Xia, H.N. Alshareef, ACS Nano 8 (2014) 9531–9541.
[22] Z. Wu, X. Pu, X. Ji, Y. Zhu, M. Jing, Q. Chen, F. Jiao, Electrochim. Acta 174 (2015) 238–245.
[23] H. Chen, J. Jiang, L. Zhang, H. Wan, T. Qi, D. Xia, Nanoscale 5 (2013) 8879–8883.
[24] J. Bao, X. Zhang, B. Fan, J. Zhang, M. Zhou, W. Yang, X. Hu, H. Wang, B. Pan, Y. Xie, Angew. Chem. Int. Ed. 54 (2015) 7399–7404.
[25] M. Zhou, F. Lu, B. Chen, X. Zhu, X. Shen, W. Xia, H. He, X. Zeng, Mater. Lett. 159 (2015) 498–501.

[26] J. Pu, F. Cui, S. Chu, T. Wang, E. Sheng, Z. Wang, A.C.S. Sustain, Chem. Eng. 2 (2013) 809–815.
[27] C. Yang, Z.F. Zhou, J.W. Li, X.X. Yang, W. Qin, R. Jiang, N.G. Guo, Y. Wang, C. Q. Sun, Nanoscale 4 (2012) 1304–1307.
[28] H. Wang, S. Lu, Y. Chen, L. Han, J. Zhou, X. Wu, W. Qin, J. Mater. Chem. A 3 (2015) 23677–23683.
[29] S. Lyapin, A. Utyuzh, A. Petrova, A. Novikov, T. Lograsso, S. Stishov, J. Phys. - Condens. Matter 26 (2014) 396001/1–396001/7.
[30] L. Zhu, D. Susac, M. Teo, K. Wong, P. Wong, R. Parsons, D. Bizzotto, K. Mitchell, S. Campbell, J. Catal. 258 (2008) 235–242.
[31] K. Andersson, M. Nyberg, H. Ogasawara, D. Nordlund, T. Kendelewicz, C. S. Doyle, G.E. Brown, L.G.M. Pettersson, A. Nilsson, Phys. Rev. B 70 (2004) 195404/1–195404/5.
[32] C.-Y. Chen, Z.-Y. Shih, Z. Yang, H.-T. Chang, J. Power Sources 215 (2012) 43–47.
[33] M. Zhou, F. Lu, X. Shen, W. Xia, H. He, X. Zeng, J. Mater. Chem. A 3 (2015) 21201–21210.
[34] T. Peng, Z. Qian, J. Wang, D. Song, J. Liu, Q. Liu, P. Wang, J. Mater. Chem. A 2 (2014) 19376–19382.
[35] X. Li, Q. Li, Y. Wu, M. Rui, H. Zeng, ACS Appl. Mater. Interfaces 7 (2015) 19316–19323.
[36] J. Yang, C. Yu, X. Fan, S. Liang, S. Li, H. Huang, Z. Ling, C. Hao, J. Qiu, Energy Environ. Sci. (2016), http://dx.doi.org/10.1039/C5EE03633J.
[37] L. Shen, J. Wang, G. Xu, H. Li, H. Dou, X. Zhang, Adv. Energy Mater. (2015), http://dx.doi.org/10.1002/aenm.201400977.
[38] L. Lin, J. Liu, T. Liu, J. Hao, K. Ji, R. Sun, W. Zeng, Z. Wang, J. Mater. Chem. A 3 (2015) 17652–17658.
[39] D. Cai, D. Wang, C. Wang, B. Liu, L. Wang, Y. Liu, Q. Li, T. Wang, Electrochim. Acta 151 (2015) 35–41.
[40] R. Ding, M. Zhang, Y. Yao, H. Gao, J. Colloid Interface Sci. 467 (2016) 140–147.
[41] T. Zhu, G. Zhang, T. Hu, Z. He, Y. Lu, G. Wang, H. Guo, J. Luo, C. Lin, Y. Chen, J. Mater. Sci. 51 (2015) 1903–1913.
[42] W. Hu, R. Chen, W. Xie, L. Zou, N. Qin, D. Bao, ACS Appl. Mater. Interfaces 6 (2014) 19318–19326.
[43] Y.X. Zhou, H.B. Yao, Y. Wang, H.L. Liu, M.R. Gao, P.K. Shen, S.H. Yu, Chem. - Eur. J. 16 (2010) 12000–12007.
[44] S. Liu, C. Mao, Y. Niu, F. Yi, J. Hou, S. Lu, J. Jiang, M. Xu, C. Li, ACS Appl. Mater. Interfaces 7 (2015) 25568–25573.
[45] J.-C. Xing, Y.-L. Zhu, Q.-W. Zhou, X.-D. Zheng, Q.-J. Jiao, Electrochim. Acta 136 (2014) 550–556.
[46] J. Xu, Q. Wang, X. Wang, Q. Xiang, B. Liang, D. Chen, G. Shen, ACS Nano 7 (2013) 5453–5462.
[47] X. Xiong, G. Waller, D. Ding, D. Chen, B. Rainwater, B. Zhao, Z. Wang, M. Liu, Nano Energy 16 (2015) 71–80.
[48] Z.-F. Huang, J. Song, K. Li, M. Tahir, Y.-T. Wang, L. Pan, L. Wang, X. Zhang, J.-J. Zou, J. Am. Chem. Soc. 138 (2016) 1359–1365.
[49] L. Shen, L. Yu, H.B. Wu, X.-Y. Yu, X. Zhang, X.W. Lou, Nat. Commun. 6 (2015) 6694/1-8.
[50] Y. Li, L. Cao, L. Qiao, M. Zhou, Y. Yang, P. Xiao, Y. Zhang, J. Mater. Chem. A 2 (2014) 6540–6548.

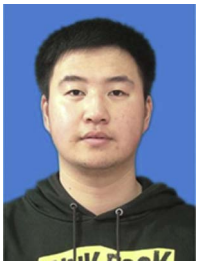

Fei Lu received his B.S. degree (2014) in microelectronics from Yangzhou University, China. Now he is a M.S. degree candidate in Yangzhou University. His current research focuses on the nano/micro-structured materials for electrochemical capacitors.

Min Zhou received his B.S. (2007) and Ph.D. (2012) degrees from Lanzhou University, China. Since then he works in College of Physical Science and Technology, Yangzhou University, China. Currently he is a visiting scholar in Prof. Bando Yoshio's group in National Institute for Materials Science (NIMS), Japan. His research focuses on the designed synthesis of non-precious nanomaterials for electrochemical energy storage and conversion devices.

Wanrong Li is a B.S. degree candidate in microelectronics in Yangzhou University, China. She is going to work toward M.S. degree in Yangzhou University. Her current research includes nanomaterials for Li-ions batteries and solar cell.

Cuiling Li received her Ph.D. degree from Changchun Institute of Applied Chemistry (CIAC), Chinese Academy of Sciences (CAS), China in 2012. Since then she started postdoctoral work with Prof. Yusuke Yamauchi supported by JSPS Postdoctoral Fellowship in National Institute for Materials Science (NIMS), Japan. Her research interests focus on the tailored design and synthesis of nanostructured metals and their applications in energy conversion systems, electrocatalysis, and analytical applications.

Yanming Xue received his Ph.D. in Materials Physics and Chemistry in 2014 from the Institute of Materials Science and Engineering, Hebei University of Technology. Now he is a postdoctoral fellow of Prof. Dmitri Golberg's group at the National Institute for Materials Science (NIMS). His current research topic is the controlled fabrication, novel properties and engineering applications of boron nitride nanotubes and nanosheets.

Xiangfen Jiang received M.S. degree from Nanjing University in 2009 for the work on hierarchically structured nitrogen-doped carbon nanocages in the group of Profs. Zheng Hu and Xizhang Wang. And she worked on mesoporous metal oxide thin films under the supervision of Prof. Yusuke Yamauchi and received Ph.D. degree from Waseda University in 2013. Then she joined Prof. Yoshio Bando's group as a postdoctoral researcher in International Center for Materials Nanoarchitectonics (MANA) of National Institute for Materials Science (NIMS). Her current research interest is fabricating porous structures of boron nitride nanosheets and carbon-based nanosheets for environmental science and energy conversion.

Xianghua Zeng is the director of the Institute of Optoelectronic Technology, and a professor of Physics in Yangzhou University, China. She received her B.S. and Ph.D. degrees from Institute of Modern Physics, Chinese Academy of Sciences. Her recent researches focus on low dimensional materials and their applications including the mechanism of the optoelectronic properties, and the performance of the cells, and supercapacitors.

Professor Yoshio Bando is a Fellow of National Institute for Materials Science (NIMS) and a Chief Operating Officer (COO) of International Center for Materials Nanoarchitectonics (WPI-MANA). He received a Ph.D. degree at Osaka University in 1975 and joined the National Institute for Research in Inorganic Materials (at present NIMS) the same year. His current research concentrates on synthesis and property of novel inorganic 1D/2D nanomaterials and their in-situ TEM analysis. He has been selected as ISI Highly Cited Researchers in Materials Science in 2014 and 2015.

Dmitri Golberg obtained a Ph.D. degree from the Ferrous Metallurgy Institute, Moscow, in 1990, and joined NIMS, 5 years later. He is a Group Leader and a Principal Investigator within MANA-NIMS, and a Professor of Tsukuba University. He has authored >600 articles cited over 25000 times (H-84), and 100+ patents. In 2005 he received the Tsukuba Prize, in 2012 - the Thomson Reuters Research Front Award, in 2014 - the "Seto" Award from the Japanese Microscopy Society, in 2014/2015 - the ISI Highly Cited Researcher, and in 2016 - the NIMS President Prize. His research focuses on nano-property studies in TEM.